J. Fluid Mech. (2005), *vol.* 545, *pp.* 141–162.
doi:10.1017/S0022112005006397 Printed in the United Kingdom

Energetic spanwise modes in the logarithmic layer of a turbulent boundary layer

By C. D. TOMKINS† AND R. J. ADRIAN

Department of Theoretical and Applied Mechanics, University of Illinois at Urbana-Champaign, Urbana, IL 61801, USA

(Received 26 January 2004 and in revised form 1 June 2005)

The influence of large-scale outer-region motions on the properties and processes of the inner layer remains an open issue in wall turbulence research. In the present work, two-dimensional power spectra of the streamwise component are measured in streamwise–spanwise planes throughout the logarithmic region of smooth flat-plate turbulent boundary layers at $Re_\theta = 1015$ and 7705. The spectra are based on PIV measurements with a wide spanwise view ($z/\delta > 2.5$), and the spanwise energy distribution is emphasized. The spectra reveal that the mode associated with the spacing of the low-speed streaks near the wall, $\lambda_z^+ \approx 100$, contains surprisingly little energy relative to modes in the range $\lambda_z^+ \approx 200$–400 at $y^+ = 21$. This result is consistent with measurements in a channel flow (Liu *et al.* 1996) at a similar height. Further from the wall, large-scale structures that scale with outer variables organize with spacing $\lambda_z/\delta = 0.75$–0.9, and these motions dominate the spanwise distribution of streamwise energy throughout the logarithmic region. The large spanwise modes are associated with the large streamwise modes on average, as the median energetic spanwise mode increases roughly linearly with increasing streamwise mode up to approximately $\lambda_{z,\mathrm{med}}/\delta \approx 0.8$, and then remains roughly constant for larger streamwise modes. The aspect ratio $\lambda_x/\lambda_{z,\mathrm{med}}$ decreases with increasing distance from the wall, suggesting that the most streaky structures remain buried near the wall.

1. Introduction

It is well known that low- and high-speed streaks exist in the near-wall region of turbulent wall flows. Previous investigations have typically used flow visualization to investigate streak spacing and characteristics, including the seminal work of Kline *et al.* (1967), who identified the mean spanwise spacing of $\lambda_z^+ = 100$, and Smith & Metzler (1983), who showed that the spacing has a log-normal distribution and increases with distance from the wall. (Variables with superscript + are non-dimensionalized by u_τ, the wall friction velocity, and $y^* = \nu/u_\tau$, the viscous length scale, where ν is the kinematic viscosity.) As a result of these and numerous other studies, the near-wall spanwise streak spacing of $\lambda_z^+ = 100$ is universally accepted, and generally considered one of the successes of turbulence structure research.

In the outer region, large-scale motions have been documented, though their spanwise spacing has received less attention than the near-wall structures. At low to moderate Reynolds number, 'bulges' of turbulent fluid have been identified defining

† Present address: Los Alamos National Laboratory, Physics Division, Los Alamos, NM 87545, USA.

the boundary-layer edge and extending on the order of δ–2δ streamwise and 0.5δ–1.0δ spanwise, where δ is the boundary layer thickness (Nychas, Hershey & Brodkey 1973; Kovasznay, Kibens & Blackwelder 1970). More recently, at both low and high Reynolds number, Adrian, Meinhart & Tomkins (2000) observed groups of vortices aligning streamwise to create very large regions of u-momentum deficit, which typically reside in the region extending from the inner layer out to $y/\delta = 0.4$–0.6. These results are consistent with many previous observations of large- and small-scale structure.

A handful of investigations have focused on the spanwise organization and properties of motions in the logarithmic layer and above. Wark & Nagib (1991) investigated a $Re_\theta = U_\infty \theta/\nu = 4650$ boundary layer (where U_∞ is the free-stream velocity and θ is the momentum thickness) using conditional averaging over the wall-normal range $55 < y^+ < 605$ and observed 'roller-type' structures extending several δ streamwise (x) and approximately 0.5δ spanwise (z). These motions were associated with Reynolds stress production, and sweeps and ejections were observed to occur in a 'quasi-periodic' manner spanwise, even in the larger scales. Rajaee, Karlsson & Sirovich (1995) performed two-point correlations of the wall-normal and streamwise velocity with spanwise separation in a turbulent channel flow. The authors interpreted the first minimum in the streamwise velocity correlation $R_{uu}(r_z)$ to be half the streak spacing, and showed that the spacing grows roughly linearly with distance from the wall up to $y^+ \approx 80$. The first minimum in the wall-normal velocity correlation $R_{vv}(r_z)$ was interpreted to be the vortex diameter. This grew linearly with y up to $y^+ = 100$. Tomkins & Adrian (2003) performed wide-view PIV (particle image velocimetry) measurements in the streamwise–spanwise plane of a boundary layer at $Re_\theta = 7705$. Horizontal planes of data at $y/\delta = 0.2$ revealed large-scale regions of u-momentum deficit that were highly elongated in the streamwise direction and bordered by sequences of concentrated wall-normal vorticity. Regions of high-speed fluid, also elongated streamwise, typically occupied the gaps between neighbouring areas of momentum deficit. The observations are consistent with the results of Adrian *et al.* (2000) and Wark & Nagib (1991). Recently, del Alamo & Jimenez (2003) performed direct numerical simulation (DNS) of a turbulent channel at $Re_\tau = u_\tau h/\nu = 180$ and 550, where $2h$ is the channel height. The authors calculated two-dimensional spectra and observed very-large-scale motions that may extend over $5h$ streamwise and up to approximately $2h$ spanwise; velocity correlations suggest that these motions penetrate down into the buffer layer. del Alamo *et al.* (2004) analysed DNS results over an extended range of Reynolds number (up to $Re_\tau = 1900$) and focused on scaling issues. Appropriate scaling parameters for spectra and correlations were not always consistent with self-similarity: they concluded that the largest streamwise wavelengths varied as λ_z^2 and were found to scale with the centreline velocity of the channel.

Scaling studies of two-point correlation functions with spanwise separation are in general agreement. McLean (1990) performed two-point correlations of streamwise velocity as a function of wall-normal distance over a significant range of Reynolds numbers ($1500 < Re_\theta < 10\,290$). The author found that $R_{uu}(r_z)$ scales with outer variables throughout the boundary layer except for small separations in the region $y^+ < 40$. Wark, Naguib & Robinson (1991) investigated the behaviour of the correlation function $R_{\tau u}(r_z)$, where τ is the streamwise wall shear stress, over the Reynolds number range $670 < Re_\theta < 5961$. The correlation was found to scale with outer units for all displacements and wall-normal locations, with the exception of displacements less than $r_z^+ = 40$ very near the wall ($y^+ \approx 10$–15).

The aim of the present work is to investigate the energy contribution and growth of these large- and small-scale structures as a function of distance from the wall in

$Re_\theta = \theta U_\infty/\nu$	1015	7705
$Re_\delta = \delta U_\infty/\nu$	8743	61863
U_∞ (m s^{-1})	1.77	11.39
δ (mm)	76.2	83.1
θ (mm)	8.84	10.35
δ^* (mm)	12.3	14.4
u_τ (m s^{-1})	0.086	0.41
y^* (mm)	0.179	0.0375
δ^+	426	2216
H(δ^*/θ)	1.391	1.391
δ/θ	0.116	0.125

TABLE 1. Smooth-wall boundary-layer flow parameters.

a zero-pressure-gradient flat-plate turbulent boundary layer at $Re_\theta = 1015$ and 7705. Particle image velocimetry (Adrian 1991) measurements are made in streamwise–spanwise planes at several wall-normal locations (see table 2 below) at each Reynolds number. The measurements have a wide field of view spanwise to capture a wide range of modes and a large number of samples for good statistical convergence. The $Re_\theta = 1015$ flow offers a similar value of $Re_\tau = u_\tau\delta/\nu = 426$ as the Liu, Adrian & Hanratty (1996) channel flow in which comparable measurements were performed. The $Re_\theta = 7705$ boundary layer is chosen to match the flow in Adrian *et al.* (2000). It contains a significant overlap region ($y/\delta = 0.2$ is equivalent to $y^+ = 440$) and a wide range of scales ($\delta^+ \approx 2200$).

2. Experiment

Measurements are performed in a low-turbulence open-circuit Eiffel-type wind tunnel. Flow is drawn in through a series of screens and honeycombs and accelerated into the test section, in which the free-stream turbulence intensity is estimated to be 0.16 %. The boundary layer develops over a smooth flat plate with dimensions 6096 mm streamwise (x) by 914 mm spanwise (z); this width is greater than ten times the boundary-layer thickness so side effects are minimal. The layer is tripped with a 4.7 mm diameter rod laid flat along the plate at $x = 110$ mm. The centre of the measurement volume is located at $x = 5310$ mm from the leading edge. A thorough description of the facility is given in Meinhart (1994).

Two Reynolds numbers are considered, $Re_\theta = U_\infty\theta/\nu = 1015$ and 7705. The experiment is designed to closely match two sets of x–y-plane measurements in Adrian *et al.* (2000). Table 1 shows flow parameters for the two cases calculated from the x–y measurements. The momentum thickness is calculated by numerically integrating the boundary-layer profile, the wall friction velocity u_τ is estimated using the Clauser (1956) chart method, and the boundary-layer thickness δ is calculated using the 0.99 criterion.

Two-dimensional velocity measurements are obtained in x–z-planes at several y-locations using digital PIV. Relevant measurement parameters are summarized in table 2. Comparison between Reynolds numbers is possible when y/δ is approximately 0.05, 0.1, and 0.2. The experiments are designed to capture a wide field of view, particularly in the spanwise direction, which extends 6090 viscous wall units in the high Reynolds number case and 1085 inner units at the low Reynolds number.

Re_θ	y^+	y/δ	Field of view $L_x/\delta \times L_z/\delta$	Field of view $L_x^+ \times L_z^+$	Number of Realizations
1015	21	0.05	1.08×2.55	460×1085	201
1015	46	0.11	1.08×2.55	460×1085	201
1015	92	0.22	1.08×2.55	460×1085	201
7705	100	0.045	1.4×2.75	3100×6090	201
7705	220	0.10	1.4×2.75	3100×6090	201
7705	330	0.15	1.4×2.75	3100×6090	201
7705	440	0.20	1.4×2.75	3100×6090	201

TABLE 2. Smooth-wall x–z-plane measurement parameters.

Double-exposed images are captured using two 2k by 2k Kodak Megaplus CCD cameras set side-by-side, giving a 2:1 spanwise–streamwise view aspect ratio with a 4k by 2k pixel array.

The images are registered mechanically using a calibration target and micro-adjustments to camera position. Camera alignment is to within 1 pixel out of 2000 vertically, horizontally, and with respect to rotation. Images are combined before interrogation. To eliminate wide-view distortions the imaging lens is an enlarging lens placed backwards in the system. Olive-oil particles of nominal 1–2 micron diameter are illuminated using two Nd:YAG pulsed lasers that produce approximately 150 mJ per pulse @ 532 nm. The laser beam is spread using negative cylindrical lenses into a sheet of 130 mm in the test section, crossing the flow in the spanwise direction. The sheet is focused using a positive spherical lens to a waist near the middle of the test section; its greatest thickness in the field of view is roughly 0.5 mm. The sheet is aligned parallel to the boundary-layer plate using alignment blocks with thin grooves precisely machined at specified heights. Light is scattered from particles through a glass plate in the test section floor to a 45° angled mirror underneath the tunnel, and collected by the lenses described above. The timing of the lasers and cameras is controlled by a TSI, Inc. synchronizer box, and the time between pulses is set at 300 μs and 100 μs for the low and high Reynolds number, respectively, resulting in average particle image displacements in the range 11–15 pixels.

The interrogation is performed using single-frame cross-correlation of double-exposed images with a discrete window offset specified *a priori*. The interrogation is carried out using PIV Sleuth software (Christensen, Soloff & Adrian 2000). Image shifting is not necessary at these locations in this zero-pressure-gradient layer because the velocities never approach zero. Slightly rectangular spots are used for the first window to improve resolution in the spanwise direction (sizes are slightly shorter in z): 36 by 44 pixels in the low Reynolds number case, and 32 by 40 pixels at the high Reynolds number. The second window is 64 by 64 pixels in both cases, and the first window is zero-padded to this size for correlation via FFTs. The second window is offset to place the correlation peak near the centre of the correlation plane, and hence remove bias due to edge effects. The particle image diameter d_τ is, on average, 3 pixel diameters, giving d_τ/d_{pix} sufficiently large to minimize bias errors due to image discretization (Adrian 1997; Westerweel 1997). Peak fitting is done using one-dimensional Gaussian three-point estimation.

This paper is concerned principally with the co-spectral distribution of energy. In the idealized flow the velocity is statistically homogeneous in the x- and z-directions, and the two-point spatial correlation function with separation (r_x, r_z) in the x–z-plane

is given by

$$R_{ij}(r_x, r_z; y) = \langle u_i'(x, y, z, t) u_j'(x + r_x, y, z + r_z, t) \rangle. \tag{2.1}$$

The primes denote velocity fluctuations from the long-term mean velocity,

$$u_i' = u_i - \langle u_i \rangle, \tag{2.2}$$

and angled brackets denote an average over an infinite ensemble. The co-spectral power density tensor is defined as

$$\Phi_{ij}(k_x, k_z; y) = \int_{-\infty}^{\infty} \int_{-\infty}^{\infty} R_{ij} \mathrm{e}^{-j(k_x r_x + k_z r_z)} \, \mathrm{d}r_x \, \mathrm{d}r_z, \tag{2.3}$$

where k_x and k_z are the streamwise and spanwise wavenumbers, respectively. The wavenumber k is related to the wavelength λ by $k = 2\pi/\lambda$. The inverse Fourier transform gives

$$R_{ij}(r_x, r_z; y) = \frac{1}{4\pi^2} \int_{-\infty}^{\infty} \int_{-\infty}^{\infty} \Phi_{ij} \mathrm{e}^{j(k_x r_x + k_z r_z)} \, \mathrm{d}k_x \, \mathrm{d}k_z, \tag{2.4}$$

from which the Reynolds stress tensor is obtained as

$$\langle u_i u_j \rangle = \frac{1}{4\pi^2} \int_{-\infty}^{\infty} \int_{-\infty}^{\infty} \Phi_{ij} \, \mathrm{d}k_x \, \mathrm{d}k_z. \tag{2.5}$$

Measurements of any of the ideal quantities defined above are always estimates of the ideal by virtue of a number of real limitations, including finite spatial resolution and accuracy of the velocity measurements, finite number of realizations in the statistical ensemble, and finite spatial extent of the measured fields.

The measurement volume in the fluid is determined by the dimensions of the interrogation spot size in x and z and the light sheet thickness in y. In terms of viscous wall units the (x,y,z) dimensions of the measurement volume are (14,2.8,11) at $Re_\theta = 1015$ and (60,13,48) at $Re_\theta = 7705$. The velocity measured by PIV, denoted by $\tilde{u}_i(\boldsymbol{x}, t)$, is an average over this volume (Adrian 1988). Fifty percent overlap of interrogation spots yields measurement resolution of 5.6 viscous units in z by 7 viscous units in x at the low Reynolds number, and 24 viscous units in z by 30 viscous units in x at the high Reynolds number. Clearly, the resolution is insufficient to resolve all of the scales of the turbulence. At each Reynolds number, however, the measurements resolve the structures of interest, while simultaneously capturing large scales. The above procedure yields approximately 20 000 and 25 000 vectors at the low and high Reynolds number, respectively. The raw fields are validated by systematic removal of bad vectors and replacement with 2nd and 3rd choices in the correlation plane where appropriate. One pass of interpolation given a high percentage of neighbouring valid measurements is performed, and finally a narrow Gaussian filter is applied to remove spatial high-frequency noise.

Statistical quantities in the current measurements are calculated by ensemble averaging over all realizations, and then averaging over the homogeneous z-direction and the nearly homogeneous x-direction. The average over all realizations is effectively a time average, and the combined operation of time averaging and spatial averaging will be denoted by an overbar. The experimental mean velocity $\overline{\tilde{u}_i}$ closely approximates the true mean. The fluctuation of the measured velocity is then

$$\tilde{u}_i' = \tilde{u}_i - \overline{\tilde{u}_i}. \tag{2.6}$$

There is a subtle point here that bears some discussion. Suppose that one chose to define the fluctuation by subtracting the spatial mean of each PIV velocity field,

instead of the combined spatial–temporal mean defined above. Each spatially averaged mean contains fluctuations due to wavelengths that are greater than the dimensions (L_x, L_z) of the PIV frame, and wavelengths that are not integer fractions, i.e. $n\lambda_i = L_i$. One can easily visualize the spatial means fluctuating from one temporal sample to the next as they ride up and down long-wavelength fluctuations. Subtracting the spatial mean removes the contributions of these long and non-integer wavelengths, so that the fluctuation is effectively high-pass filtered. Since we are interested in the contribution of the largest scales, this sort of filtering must be avoided. By taking the long-time average of the spatial means as our reference, the fluctuations contain contributions from all wavelengths. We will see later that this means that the spectra contain information (albeit distorted) down to zero wavenumber, even though the length of the PIV data domain is finite.

The measured two-point spatial correlation function is denoted by

$$\hat{\tilde{R}}_{ij}(r_x, r_z; y) = \overline{\tilde{u}'_i(x, y, z, t)\tilde{u}'_j(x + r_x, y, z + r_z, t)}, \tag{2.7}$$

where the overbar denotes the aforementioned space–time average, and the carat emphasizes that (2.7) is only an estimate of the ideal correlation given by (2.1).

Experimentally, the ideal power spectral density functions must be estimated from a finite set of data realizations measured on a finite spatial domain with finite spatial resolution. Following conventional practice, we estimate the power spectral density by Fourier analysing the windowed velocity data from each PIV frame, forming the product of the Fourier coefficients, and time averaging. Specifically, a Hanning window function

$$w_H(x', z') = \begin{cases} C_H \left[1 - \cos^2\left(\dfrac{\pi x'}{L_x}\right)\right]\left[1 - \cos^2\left(\dfrac{\pi z'}{L_z}\right)\right] & \text{for } x \leqslant x' \leqslant x + L_x, \\ & z \leqslant z' \leqslant z + L_z \\ 0 & \text{otherwise} \end{cases} \tag{2.8}$$

(with the constant C_H adjusted to assure proper energy conservation) is applied to the velocity data in each PIV frame. The Fourier transform

$$\begin{aligned} F[w_H\tilde{u}'_i] &= \int_{-\infty}^{\infty}\int_{-\infty}^{\infty} \mathrm{e}^{-j(k_x x' + k_z z')} w_H(x', z')\tilde{u}'_i(x', y, z')\,\mathrm{d}x'\,\mathrm{d}z' \\ &= \int_{x}^{x+L_x}\int_{z}^{z+L_z} \mathrm{e}^{-j(k_x x' + k_z z')} w_H(x', z')\tilde{u}'_i(x', y, z')\,\mathrm{d}x'\,\mathrm{d}z' \end{aligned} \tag{2.9}$$

is computed by discrete Fourier transform using zero padding to increase the spectral resolution. The estimate of the co-spectral density tensor is calculated from the discrete Fourier transforms according to

$$\hat{\tilde{\Phi}}_{ij} = \overline{F^*[w_H\tilde{u}'_i]F[w_H\tilde{u}'_j]}. \tag{2.10}$$

It can be shown by straightforward calculation that the ensemble average of (2.10) converges to

$$\langle\hat{\tilde{\Phi}}_{ij}\rangle = \int_{-\infty}^{\infty}\int_{-\infty}^{\infty} \mathrm{d}k'_x\,\mathrm{d}k'_z \tilde{\Phi}_{ij}(k_x, y, k_z)|F[w_H](k_x - k'_x, k_z - k'_z)|^2 \tag{2.11}$$

where $\tilde{\Phi}_{ij}$ is the co-spectral density tensor of $\tilde{\boldsymbol{u}}$, the measured velocity. The estimate is smoothed by a window function in wavenumber space that is determined by the Fourier transform of the Hanning window. According to Bendat & Piersol (1986), the width of the spectral window in k_i is approximately $4\pi/L_i$, $i = 1, 2$. Thus, the

wavenumbers of order of the fundamental, $2\pi/L_i$, or less are not well resolved. Interestingly, (2.11) allows for evaluation of the spectral energy density at wavelengths longer than L_x or L_z, extending even to infinity. As explained earlier, this is possible because the fluctuations contain energy from wavelengths greater than the data domain. However, the smoothing is substantial, so for wavenumbers less than several times $2\pi/L_i$ the spectral estimate should be interpreted as a combination of the energies of neighbouring modes in wavenumber space.

The spectral estimate in (2.11) is attenuated at high wavenumbers by the averaging over the PIV measurement volume (dimensions $D_x \times D_z$) that is implicit in $\tilde{\boldsymbol{u}}$. The attenuation in the spanwise direction becomes greater than approximately 60 % for wavenumbers above $k_z^+ = 21$ and 97 for the low and high Reynolds number case, respectively. The energy attenuation factor due to a simple uniform average in direction x_i is

$$|H(k_i, D_i)|^2 = \frac{2}{(k_i D_i)^2}\,(1 - \cos(k_i D_i)), \quad i = x, y, z; \text{ no sum on } i. \tag{2.12}$$

These factors have been used to correct for attenuation by dividing the spectral estimate by appropriate combinations, e.g.

$$\hat{\Phi}_{ij}(k_x, y, k_z) \cong \hat{\tilde{\Phi}}_{ij}(k_x, y, k_z)/|H(k_x, D_x)||H(k_z, D_z)|. \tag{2.13}$$

The attenuation is negligible (i.e. $|H|^2$ is near one) for the low Reynolds number case except near the largest wavenumbers. Above this wavenumber the spectra are considered unreliable and omitted. The amount of energy contained in the omitted range is negligible. In the high Reynolds number case, the attenuation at a given k_i^+ is more severe due to the diminished viscous length scale. However, the wavenumber range of attenuated energy remains well above the wavenumber range of highly energetic modes due to the shift of energy towards larger-scale motions, in terms of viscous wall units, as the Reynolds number is increased. (This will be evident in subsequent figures.)

3. Results and discussion

Figure 1 shows good agreement between the mean streamwise velocity measured at each height and the mean velocity profile found in Adrian *et al.* (2000) for each Reynolds number. Near the logarithmic region all four sets of data converge, as expected. Root-mean-square streamwise velocity measurements also agree with the Adrian *et al.* (2000) results to within 7 % and 3 % for the low and high *Re*, respectively.

Most previous determinations of mean streak spacing have been performed by flow visualization. Here the mean streak spacing is taken to be the reciprocal of the average number of streaks per unit width over all realizations at a given height. The results of this procedure are plotted in figure 2, along with a group of results from other researchers collected by Kasagi (1988). The present results and the results of Liu *et al.* (1996), found by counting low-speed streaks in PIV vector fields, are clearly consistent with the relatively wide range of data previously observed. As expected, the streak spacing starts around $\lambda_z^+ = 100$ very near the wall and increases with y. At $y^+ = 21$, the mean spacing is approximately $\lambda_z^+ = 130$–135.

While the collected data obtained through flow visualization are impressively consistent, it is important to realize that streak identification by eye emphasizes the smaller scales, due to the characteristics of subjective human perception. The planar

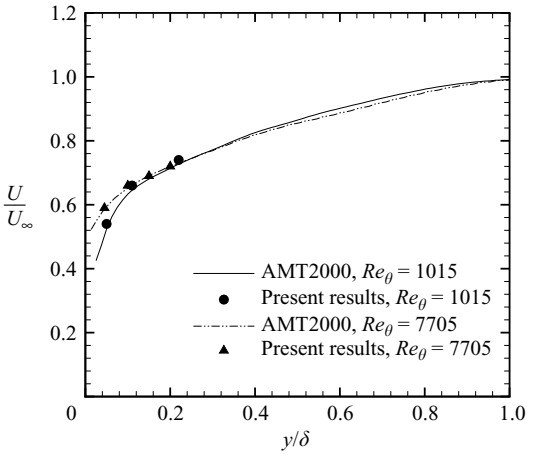

FIGURE 1. Mean streamwise velocity for each data set plotted and scaled in outer variables. Included are profiles from the x–y-plane results of Adrian *et al.* (AMT 2000).

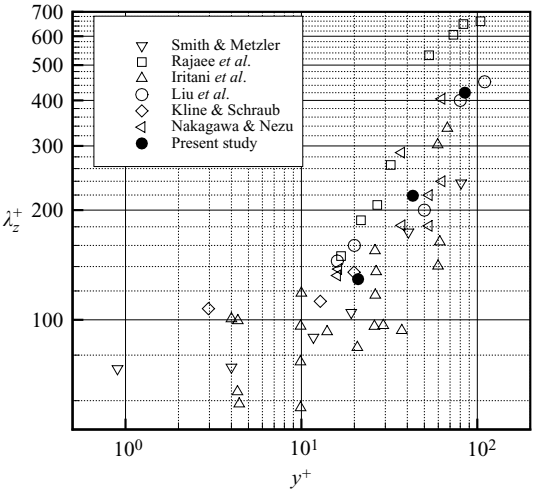

FIGURE 2. Mean spanwise spacing of low-speed streaks as a function of wall-normal location plotted in inner variables. The spacing is estimated by counting streaks visually. Included are the channel flow results of Liu *et al.* (1996), and several other studies originally compiled by Kasagi (1988).

PIV data, however, allow objective and quantitative analysis via two-dimensional power spectra of the streamwise velocity in horizontal planes.

3.1. *Low Reynolds number spectra*

Contours of two-dimensional spectra of the streamwise component are presented in figure 3 for $Re_\theta = 1015$ and 7705. The spectra show that the regions of highest energy in the streamwise direction are confined to the lowest wavenumbers, revealing the importance of the largest motions even near the wall. The low Reynolds number results reveal that in the spanwise direction the most energetic contours are in the approximate wavelength range $\lambda_z^+ = 200$–400. The mode associated with the spacing of the low-speed streaks, $\lambda_z^+ = 100$, is energetic, but it is clearly not the region of peak energy. This is consistent with the results of Liu *et al.* (1996) using film PIV

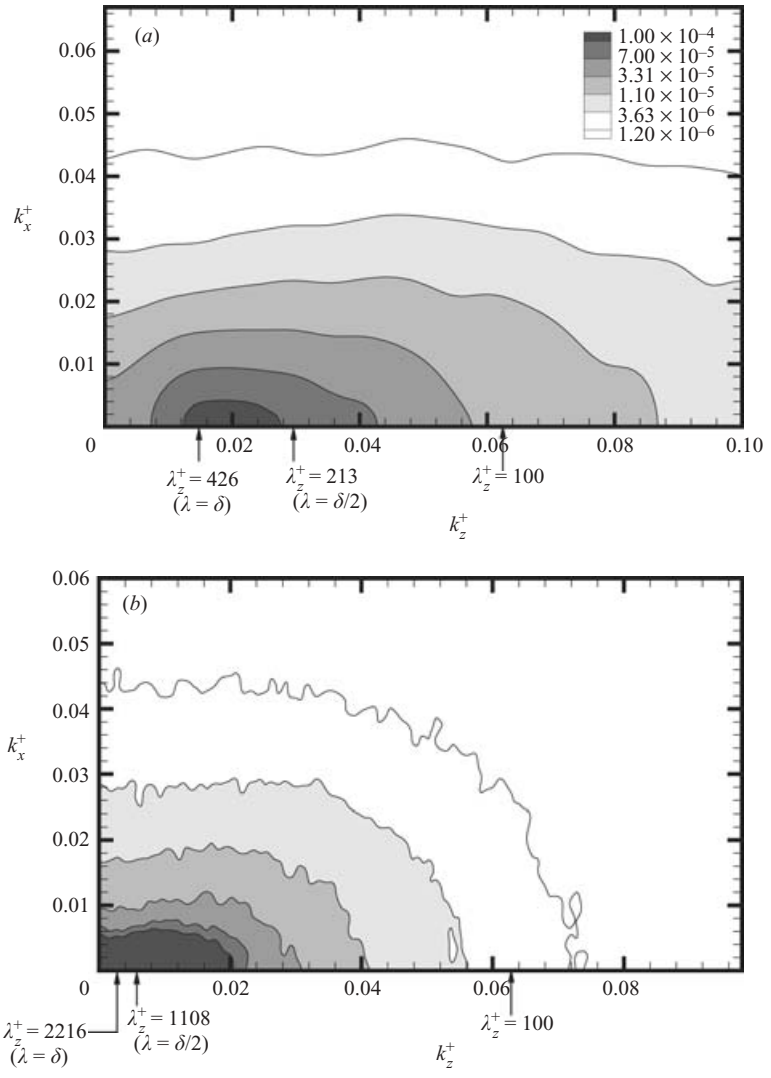

FIGURE 3. Contours of the two-dimensional spectral estimate of the streamwise component, $\hat{\Phi}_{uu}^+(k_x^+, y^+, k_z^+)$, as a function of streamwise and spanwise wavenumber, plotted in inner units. (*a*) $y^+ = 21$, $Re_\theta = 1015$. (*b*) $y^+ = 100$, $Re_\theta = 7705$.

in a turbulent channel. While it is not surprising that the peak energy is located at wavelengths greater than exactly $\lambda_z^+ = 100$ (Kline *et al.* 1967 found peak energy at $\lambda_z^+ = 130$), the scale of the energetic modes is surprising (i.e. with significant energy in the range $\lambda_z^+ \approx 200$–400). The high Reynolds number results show the energy distribution further from the wall ($y^+ = 100$). Here the regions of highest energy are confined to the lowest streamwise and spanwise wavenumbers.

An informative way of viewing two-dimensional spectra is to extract several 'slices' of data corresponding to specific streamwise wavenumbers, and observe how the energy in these particular streamwise modes varies as a function of spanwise wavenumber. This is done in figure 4, which contains data for both the Liu *et al.* channel flow (open symbols) and the low Reynolds number boundary layer (solid

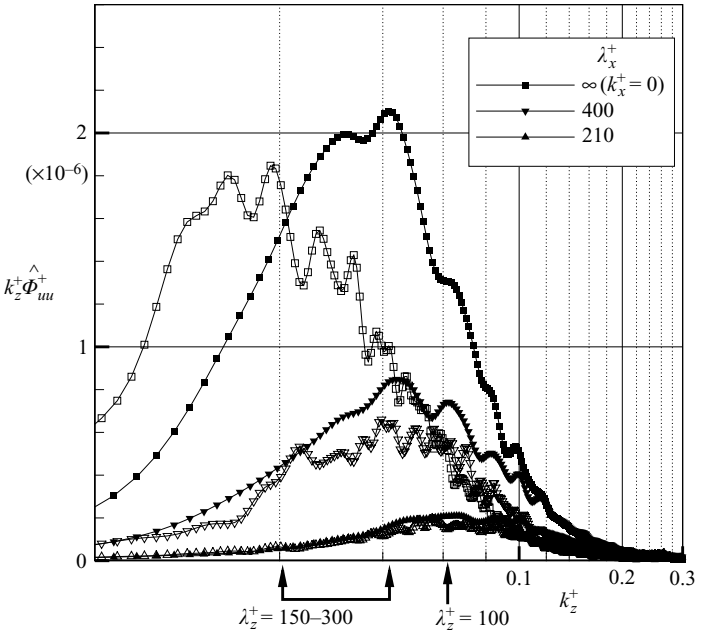

FIGURE 4. Pre-multiplied, two-dimensional spectral estimate of the streamwise component versus spanwise wavenumber for selected streamwise wavelengths at $y^+ = 21$ and $Re_\theta = 1015$ ($Re_\tau = 426$) (solid symbols). Plotted in inner units. Included are the channel flow results of Liu *et al.* (1996), open symbols, at similar streamwise wavelengths and Reynolds number ($Re_\tau = 400$).

symbols) at $y^+ = 21$. Here premultiplied power spectra of the streamwise component $k_z^+ \hat{\Phi}_{uu}^+(k_x^+, y^+, k_z^+)$ are plotted versus spanwise wavenumber, k_z^+, for several values of the streamwise wavelength, λ_x^+. Consider the spanwise variation of the streamwise modes $\lambda_x^+ = 210$. These modes represent higher-wavenumber streamwise motions with relatively low energy. Their peak energy spanwise is very near $\lambda_z^+ = 100$, but their overall energy contribution is low. Now consider the streamwise modes $\lambda_x^+ = 400$. These modes represent larger and more energetic inner-layer streamwise scales. Peak spanwise energy is in the range $\lambda_z^+ = 120$–150, centred very near the observed streak spacing of approximately $\lambda_z^+ = 135$ at this height. This is consistent with the idea that the shorter streamwise modes represent the near-wall structures, and subsequently reflect the streak spacing more closely. Furthermore, these modes (and the $\lambda_x^+ = 210$ modes) are in close agreement for both facilities, suggesting that the near-wall structures are similar. When considering all streamwise modes, however, it is seen that while $\lambda_z^+ \approx 135$ is an energetic mode, much more energy is contained in larger scales, in the range $\lambda_z^+ = 150$–300, for both the channel and boundary layer. This range is higher than one would expect based on the flow visualization estimates. The trend for energy to increase with decreasing streamwise wavenumber is clearly apparent in figure 4. Furthermore, that energy is contained in increasingly large spanwise modes as streamwise wavelength increases. Hence, the larger spanwise modes are more energetic when integrating over all streamwise wavenumbers.

A recent letter by del Alamo & Jimenez (2003) reports similar behaviour in spectra of a simulated channel flow at $Re_\tau = 550$. The authors segregate the

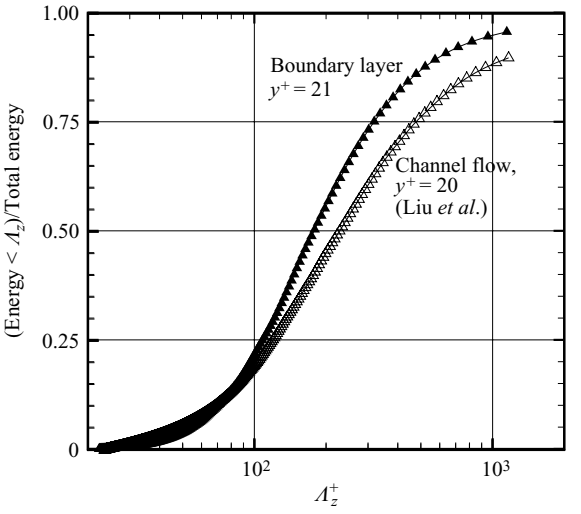

FIGURE 5. Cumulative spectral energy normalized by total energy versus spanwise wavelength plotted in inner units at $Re_\theta = 1015$ ($Re_\tau = 426$). Included are the results of Liu *et al.* (1996) ($Re_\tau = 400$). Modes greater than the field of view are omitted.

streamwise–spanwise spectra in terms of streamwise scale, and observe a shift of energy toward larger spanwise modes as streamwise wavelength increases.

The boundary layer and channel differ in the spanwise distribution of energy in the largest streamwise mode ($k_x^+ = 0$). These highly energetic streamwise modes represent the largest scales, and thus may embody differences in the facility geometry. As seen in figure 4, differences in the spanwise energy distribution of the large streamwise motions in the boundary layer and channel persist right down to $y^+ = 21$. Thus, similarity is observed in the spanwise energy distribution of the near-wall motions, represented by the higher streamwise wavenumber modes. However, the outer scales influence the energy distribution of the lower streamwise wavenumber modes, which dominate the turbulent kinetic energy even close to the wall, preventing universal behaviour over all scales. Consequently, the total streamwise energy cannot be expected to exhibit universal behaviour, even in the near-wall region.

The cumulative spectral energy contained within all spanwise modes of wavelength $\lambda_z^+ < \Lambda_z^+$ is obtained by integrating the spectra over all streamwise modes to obtain one-dimensional spectra in k_z^+, and then integrating from $k_{z,\mathrm{maximum}}^+$ down to $K_z^+ = 2\pi/\Lambda_z^+$. This quantity permits one to easily estimate the contribution to the total streamwise energy from various bands of spanwise modes. The percentage of cumulative energy in spanwise modes of wavelength less than Λ_z^+ is plotted in figure 5 for the boundary layer and channel at similar heights. Modes larger than the field of view are not plotted, though they contribute the necessary energy (≈ 5–$10\,\%$) to yield $100\,\%$ of the total energy as Λ_z^+ approaches infinity. The energy distributions for the channel and boundary layer are similar. Most strikingly, the data show that *near the wall* ($y^+ \approx 21$) *a significant fraction of the energy, greater than 75 %, is contained in modes larger than* $\lambda_z^+ = 100$. Furthermore, about $65\,\%$ of the energy is in modes greater than the value of $\lambda_z^+ = 135$ estimated by flow visualization. As spanwise scale increases, the difference between the curves increases, becoming significant for the large scales. This may again be a manifestation of the differences in the large scales imposed by the different conditions in the flow facilities.

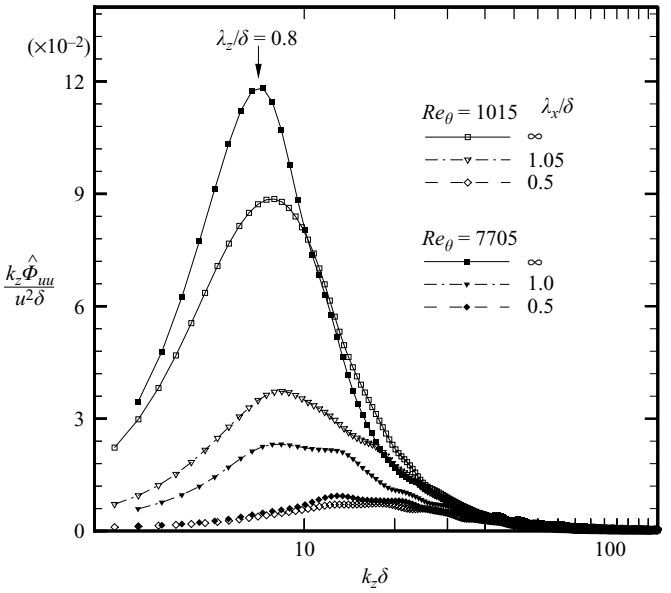

FIGURE 6. Pre-multiplied, two-dimensional spectral estimate of the streamwise component plotted versus spanwise wavenumber for selected streamwise wavelengths at $y/\delta \approx 0.2$, plotted in outer units. The results at $Re_\theta = 1015$ (open symbols) and $Re_\theta = 7705$ (solid symbols) are compared.

3.2. *High Reynolds number spectra*

The higher Reynolds number boundary layer provides a flow with a significant range of scales ($\delta^+ = 2215$) and hence a larger overlap region. Two-dimensional spectra of the streamwise component are computed at four heights throughout the logarithmic region of the layer, from $y^+ = 100$ ($y/\delta = 0.045$) up to $y/\delta = 0.2$ ($y^+ = 440$).

Previous boundary-layer studies at moderately high Reynolds number (e.g. Wark & Nagib 1991; Adrian *et al.* 2000; Tomkins & Adrian 2003) reveal large-scale, low-momentum streaks in the log-layer and above. These motions may extend many δ streamwise, and up to approximately 0.5δ–1.0δ spanwise. Measurements at the outer edge of the logarithmic region provide information about these large-scale structures. In figure 6, spectra are plotted in a similar fashion to figure 4 at both Re_θ, except, following the correlation results of McLean (1990), outer scaling is used. The streamwise wavelengths selected range from $\lambda_x/\delta = \infty$ ($k_x\delta = 0$ mode) down to $\lambda_x/\delta = 0.5$. Note that $\lambda_x/\delta = 1$ is close to the largest streamwise wavelength within the data domain for each Reynolds number. The $\lambda_x/\delta = \infty$ mode represents the contributions of all modes longer than the PIV data domain, which are aliased into it.

The plot reveals that the locations of the maxima of the spanwise energetic modes at the top of the log layer are similar for the two Reynolds numbers, in that they are both centred near $\lambda_z/\delta \approx 0.8$. Spanwise modes near this value are dominant in the largest streamwise wavelengths in the two-dimensional spectra. These large streamwise scales are most influential on the total kinetic energy, and thus the spanwise modes near $\lambda_z/\delta \approx 0.8$ persist to be the peak energetic modes in the one-dimensional k_z spectra (obtained by integrating over all streamwise modes). These $\lambda_z/\delta \approx 0.8$ modes may be interpreted to represent the average spanwise spacing of the large-scale motions in the

outer region of the flow. As discussed in Tomkins & Adrian (2003), these motions are regions of streamwise momentum deficit. Often, high-speed fluid is observed filling the spaces between neighbouring motions. This large-scale quasi-periodicity is also observed in Wark & Nagib (1991).

Unlike the spanwise modes of peak energy, a Reynolds number effect does exist in the distribution of energy among streamwise modes. Figure 6 reveals that streamwise wavelengths near $\lambda_x/\delta = 0.5$ show good agreement in spanwise energy distribution for the two Reynolds numbers. However, the largest streamwise motions (represented by the $k_x\delta = 0$ mode) contain a greater percentage of energy at $Re_\theta = 7705$ than at $Re_\theta = 1015$, although that energy is distributed similarly spanwise. At the higher Reynolds number, then, the energy is more concentrated in the largest streamwise modes.

Thus, for the outer edge of the logarithmic region, where the largest scales dominate, a picture emerges in which the large scales at both Reynolds numbers organize and find an average spanwise spacing. This spacing is revealed as a band of dominant spanwise energetic modes. How this behaviour changes as the wall is approached is of obvious interest. One-dimensional spectra in k_z at several heights in the log layer are presented in figure 7. In figure 7(*a*), the spectra are premultiplied and plotted in outer units versus the dimensionless spanwise wavenumber $k_z\delta$. The spanwise energy distribution in the outer region ($y/\delta = 0.2$) peaks near $\lambda_z/\delta = 0.8$, consistent with the two-dimensional results in figure 6. This value corresponds to a large wavelength in wall units, $\lambda_z^+ = 1900$ at $Re_\theta = 7705$. Interestingly, as the wall is approached, this outer-region mode continues to contribute dominantly to the turbulent kinetic energy. At $y/\delta = 0.15$, the energy distribution is nearly identical to that at $y/\delta = 0.2$. At $y/\delta = 0.1$, the peak energy shifts slightly towards higher wavenumbers, but still corresponds to large-scale spanwise motions ($\lambda_z^+ = 1550$, $\lambda_z/\delta = 0.7$). The energy in slightly larger wavenumbers (in the approximate range $k_z\delta > 15$) increases. Closest to the wall, at $y/\delta = 0.045$ ($y^+ = 100$), the presence of the surface becomes apparent. Higher-wavenumber motions, corresponding to wavelengths in the range $\lambda_z^+ = 200$–600, as marked, become much more energetic. Nonetheless, the large-scale modes continue to contribute significantly, and in fact still represent the peak energy. Also marked on the plot are the spanwise modes approximately corresponding to the structure spacing estimated by flow visualization at $y^+ = 100$, as summarized in figure 2. These modes are in the range $\lambda_z^+ = 400$–600; they are clearly energetic, but they only represent a fraction of the most energetic modes on the wavenumber axis. The near-wall streak spacing mode $\lambda_z^+ = 100$ is also marked. It contains relatively little energy even after correction for attenuation.

In figure 7(*b*) the same data are plotted versus $k_z y$, and it is clear from the collapse of the curves for $k_z y > 4$ that y constitutes the correct length scale for this range of wavenumbers, i.e. for wavelengths less than $\lambda_z < \frac{1}{2}\pi y$. For longer wavelengths we have already seen from figure 7(*a*) that δ is the correct length scale. Thus, the length scale of the spanwise modes grows with y across the log-layer and then saturates at a value proportional to δ, much like the usual model of the turbulent mixing length.

Further interpretation may be given to the change in behaviour at $y^+ = 100$ in figure 7(*a*). Several researchers have suggested a more restrictive definition of the log layer (e.g. Osterlund *et al.* 2000; Zagarola & Smits 1998; McKeon *et al.* 2004). The limits of Osterlund *et al.* (2000), which were developed for boundary layers, are valid for $Re_\theta > 6000$. Here, viscous effects extend further from the wall so that the layer starts at $y^+ = 200$ and continues up to $y/\delta = 0.15$. By this definition, the measurements at $y^+ = 100$ lay within the 'extended buffer' region and not the bottom of the log

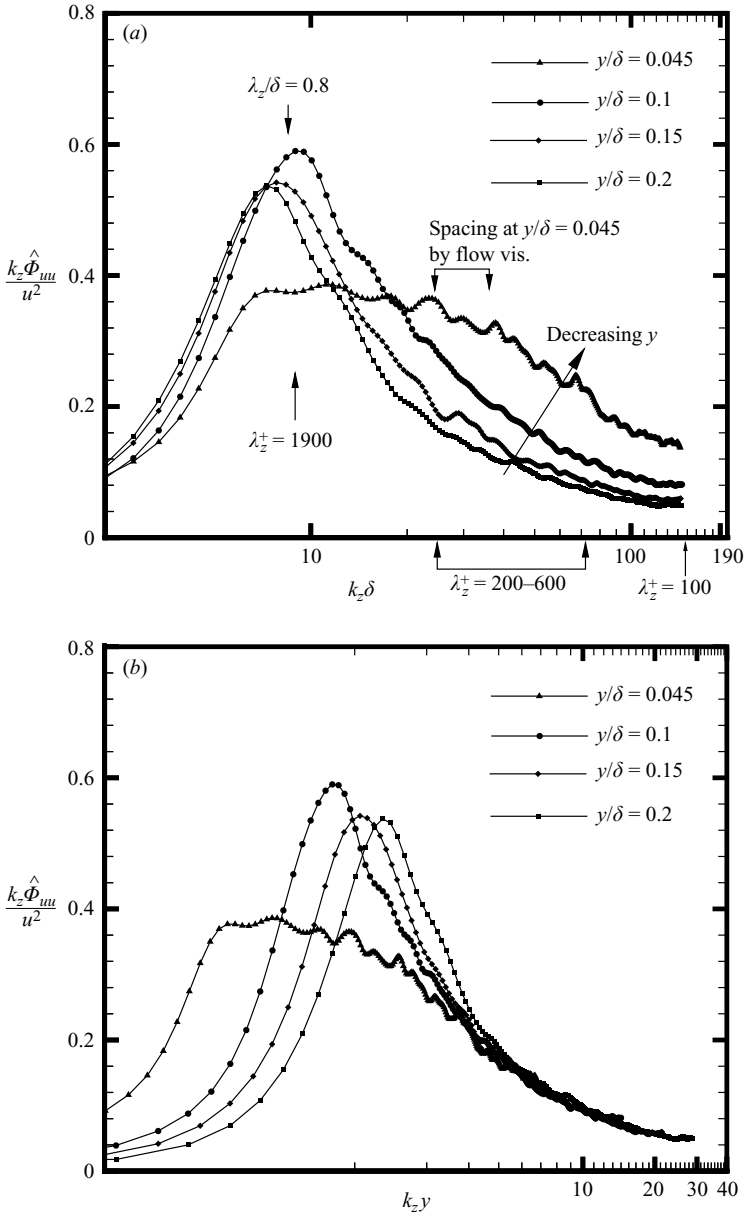

FIGURE 7. Pre-multiplied, one-dimensional spectral estimate of the streamwise component for several wall-normal locations at $Re_\theta = 7705$. (*a*) Plotted versus $k_z\delta$. (*b*) Plotted versus $k_z y$.

layer. This interpretation is consistent with the changing character, i.e. the sudden increase in energy of the moderate to smaller scales, of the $y^+ = 100$ data relative to the other data sets. The results of Zagarola & Smits (1998) and McKeon *et al.* (2004) suggest even more restrictive limits, both in terms of wall-normal location and Reynolds number, but these are for pipe flow. The present results suggest that the differences between boundary layers, channels, and pipes may be important as large-scale motions, which are affected by the geometry of the apparatus, exert influence near the wall. This is particularly true for boundary layers, as no upper wall exists.

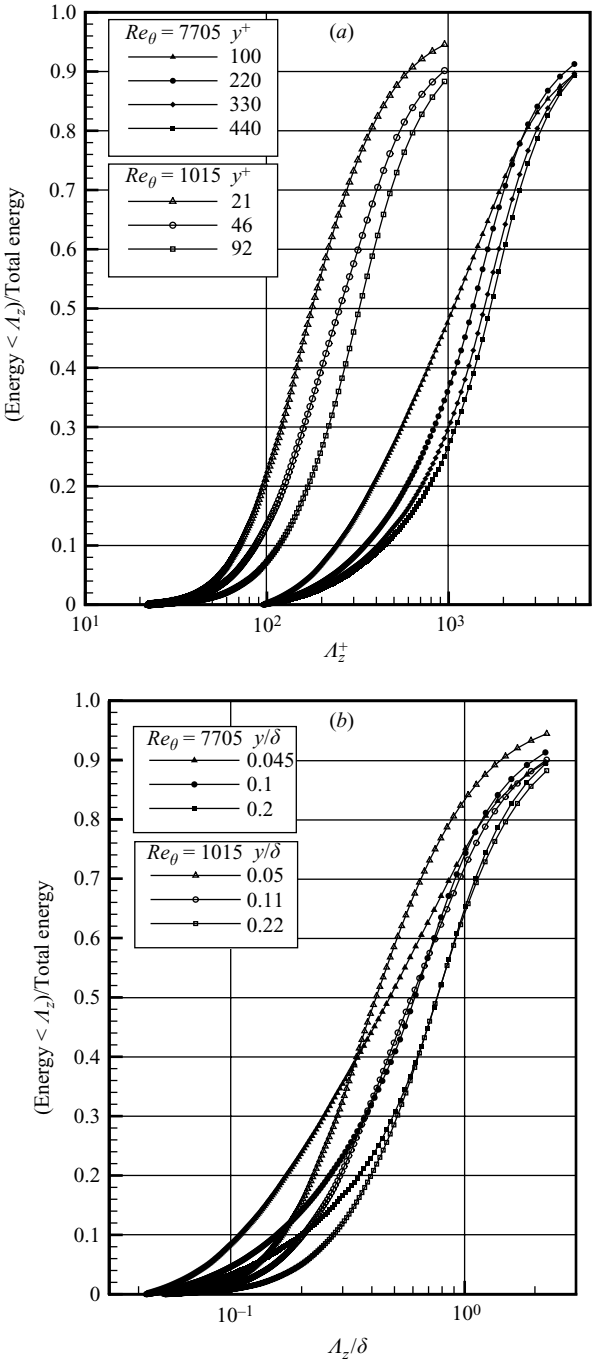

FIGURE 8. Cumulative spectral energy normalized by total energy versus spanwise wavelength for several wall-normal locations and both Reynolds numbers. (*a*) Inner units; (*b*) outer units. Modes greater than the field of view are omitted.

As discussed in the earlier section, the cumulative spectral energy contained in spanwise modes up to wavelength Λ_z may be obtained through integration of the two-dimensional spectra and plotted against Λ_z. This is done in figures 8(*a*) (inner

units) and 8(*b*) (outer units) for four wall-normal locations at the high Reynolds number and three wall-normal locations at the low Reynolds number. The cumulative energy is normalized by total energy in all cases.

The low Reynolds number curves in figure 8(*a*) (hollow symbols) show that a relatively small percentage of energy ($\approx 22\,\%$) is contained in modes whose wavelengths are less than $\lambda_z^+ = 100$ at $y^+ = 21$, as discussed earlier. As distance from the wall increases, the energy shifts towards larger scales, as expected, up to $y^+ = 92$. The high Reynolds number data, however, reveal a dramatic shift in the energy towards the large scales in plus-units: contrast, for example, the low Reynolds number curve at $y^+ = 92$ with the high Reynolds number curve at $y^+ = 100$. This shift is significant, despite the steep initial slope of the $y^+ = 100$ curve relative to the other high-*Re* data. This increased slope is a manifestation of the increased energy in the range $\lambda_z^+ = 200$–600 as seen in figure 7, and might be interpreted as evidence in favour of the modified log-layer limits of Osterlund *et al.* (2000). Flow visualization at this height reveals structure spacing of approximately $\lambda_z^+ = 500$. However, over 70 % of the turbulent kinetic energy is contained in spanwise modes larger than this. At all heights, over 50 % of the energy is in modes greater than $\lambda_z^+ = 1000$, with the percentage increasing to over 70 % at the greatest height. Thus, at the high Reynolds number, the energetic spanwise modes throughout the logarithmic region are extremely large in terms of viscous wall units.

Normalization by the boundary-layer thickness provides much better collapse of the data, as seen in figure 8(*b*), again pointing to the influence of the outer-region scales. The data at $y/\delta \approx 0.1$ and 0.2 show Reynolds number similarity for the larger scales, i.e. in the range $\Lambda_z/\delta > 0.5$. For these heights, the curves at different Re_θ begin to diverge for the smaller-scale motions. A greater percentage of energy is observed in the smaller scales of the high Reynolds number flow; this makes sense, due to the greater number of viscous wall units corresponding to a given outer length scale. Closest to the wall ($y/\delta \approx 0.05$), the results are quite different for the two Reynolds numbers. The high Reynolds number case contains more energy in the small scales, e.g. at $\Lambda_z/\delta = 0.1$. In interpreting these results, however, it is important to remember that the low Reynolds number near-wall data correspond to $y^+ = 21$, and $\lambda_z/\delta = 0.1$ corresponds to $\lambda_z^+ = 42$. Thus, in the midst of the low-speed streaks, one would not expect much energy contribution from spanwise modes near $\lambda_z^+ = 42$.

Figure 9 (inset) shows the percentage of energy in spanwise modes $\lambda_z/\delta > 0.5$ versus wall-normal location. At the outer edge of the log layer, 70 % of the energy is in the large scales at both Reynolds numbers. As the wall is approached ($y/\delta \approx 0.1$), the percentage drops to about 58 %. At $y/\delta \approx 0.05$, the large-scale energy contribution at the low Reynolds number ($y^+ = 21$) is 43 % – still quite substantial. At $Re_\theta = 7705$, the influence of the outer region structures persists. For example, 50 % of the energy is in scales $\lambda_z/\delta > 0.45$; that is, 50 % of the energy is in scales greater than or equal to 10 times the distance from the wall at $y^+ = 100$.

Figure 4 suggests a trend in which more energy resides in the low spanwise wavenumber range with increasing streamwise wavelength. Such a trend may be examined quantitatively by calculating the median spanwise energetic mode $\lambda_{z,\mathrm{med}}/\delta$ (the mode over and under which 50 % of the energy resides) for each streamwise mode. This median spanwise mode is plotted against λ_x/δ in figure 9 for each y location. The most obvious trend from the data is an increase in median spanwise mode with increasing streamwise wavelength at all heights, confirming the correlation between the scales in x and z. $\lambda_{z,\mathrm{med}}/\delta$ increases roughly linearly with λ_x/δ up to $\lambda_x/\delta \approx 1.0$. Note that the constant of proportionality varies as a function of y, possibly due

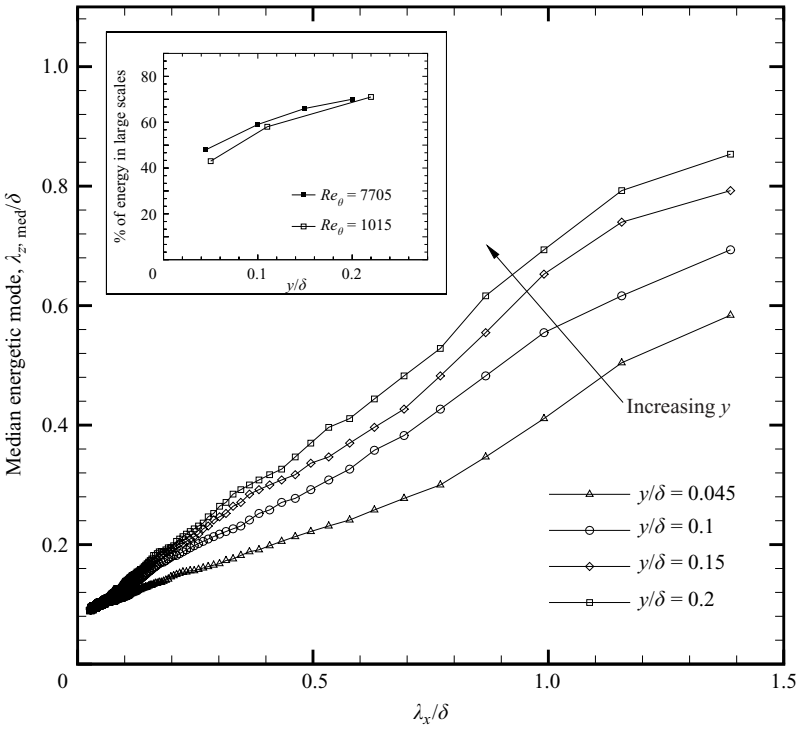

FIGURE 9. Median spanwise energetic mode as a function of streamwise mode for several wall-normal locations at $Re_\theta = 7705$, plotted in outer units. Inset: Percentage of energy in large spanwise scales ($\lambda_z/\delta > 0.5$) versus wall-normal location for both Reynolds numbers, plotted in outer units.

to a lack of streamwise similarity. Interestingly, $\lambda_{z,\mathrm{med}}/\delta$ begins to level off from linear growth for λ_x/δ greater than about one. In the field of view of the figure, this behaviour is only hinted at, but the limiting values (i.e. those associated with the $k_x = 0$ mode) of $\lambda_{z,\mathrm{med}}/\delta$ confirm it: all curves asymptote to median modes in the range $0.79 < \lambda_{z,\mathrm{med}}/\delta < 0.92$. Qualitatively similar behaviour, in terms of λ_z growing with λ_x before levelling off, was observed in the spectra of del Alamo & Jimenez (2003). del Alamo *et al.* (2004) concluded that for the largest streamwise modes λ_x grows as $\sqrt{\lambda_z}$, but the finite streamwise view of the present data does not permit confirmation of this result. The present results do suggest, however, that energetic modes grow at similar rates in x and z up $\lambda_x/\delta \approx 1$–2, and above this size they grow mainly in x.

This observation may be interpreted in terms of the large-scale, streamwise-elongated structures observed previously (e.g. Tomkins & Adrian 2003; Wark & Nagib 1991) and evident in the instantaneous fields of the present experiment. The data are consistent with a simple model in which motions grow from the wall in a roughly self-similar fashion until the large scales are densely distributed spanwise to fill the layer. At this point, they may continue to grow streamwise, corresponding to the levelling off observed in figure 9 for the largest scales. It is noteworthy that the limiting spanwise spacing of the structures roughly corresponds to the dominant spanwise modes of the outer region, near $\lambda_z/\delta = 0.8$.

The concept of vortex packets (see e.g. Head & Bandyopadhyay 1981; Smith 1984; Adrian *et al.* 2000) is also useful in interpretation. Briefly stated, these 'packets' are groups of hairpin or cane-like vortices inclined to the wall and aligned streamwise

that propagate downstream together with little velocity dispersion. In this model, the legs and head of each vortex rotate to induce a region of low-speed fluid locally. Due to the streamwise alignment, the vortices work cooperatively to create a region of low streamwise momentum as long as the packet and as wide as an individual vortex. This model provides an explanation for the existence of these streamwise-elongated large-scale motions. Furthermore, through the generation of additional vortices in the streamwise train, the packet paradigm provides a means by which the streamwise growth of the large scales may continue despite the spanwise growth limitations.

A highly idealized schematic interpretation of the energetic motions is presented in figure 10. Figures 10(*a*) and 10(*b*) depict the average growth of several motions of varying scale embedded within a δ-scale structure. In figure 10(*a*), the idealized motions are viewed in the y–z-plane; they are shown growing self-similarly in y and z, on average, consistent with the results of Tomkins & Adrian (2003). This growth continues until they reach some critical scale (possibly the scale at which motions fill the layer spanwise). In figure 10(*b*), the same set of idealized structures is viewed in the x–y-plane. Again, the motions grow self-similarly up to this critical point, after which they continue to grow streamwise. All structures remain rooted to the wall, however, consistent with the attached-eddy hypothesis (Townsend 1976). The present results do not speak to the exact nature of the motions, but they are not inconsistent with the eddy packet model suggested in Tomkins & Adrian (2003) and Adrian *et al.* (2000). Part (*c*) of the figure depicts a series of simplified large motions aligned streamwise. This concatenation of δ-scale motions is presented as a possible mechanism for the appearance of very-large-scale streamwise motions in the layer, as observed in Kim & Adrian (1999).

It is also informative to examine how the structures vary in streamwise and spanwise size with distance from the wall. For a given λ_x/δ in figure 9, $\lambda_{z,\mathrm{med}}/\delta$ increases with y. Thus, the streamwise/spanwise aspect ratio of structures, $\lambda_x/\lambda_{z,\mathrm{med}}$, appears to decrease with y location, such that the most highly elongated or streaky structures occur closest to the wall. This is consistent with previous estimates of the aspect ratio of integral length scales based on correlation measurements $R_{uu}(x, z)$ as a function of wall-normal location (Krogstad & Antonia 1994).

The results of Naguib & Wark (1992) are also consistent with the present data. The authors band-pass filtered hot-wire velocity signals in time to separate the contributions from motions of different scale, and used correlations of the filtered signals to determine scaling for each filter. They observed that the energy of outer-region structures with large streamwise scale increases with Reynolds number in the range $1579 < Re_\theta < 5961$ to 'overwhelm' the streamwise velocity fluctuations, even near the wall. The present data cover a comparable range of Reynolds number, and here it has been demonstrated that the large spanwise scales dominate the streamwise energy throughout the logarithmic layer. These two observations are consistent, and quantitatively linked by the two-dimensional spectra, as presented in figure 9, which reveal that the large streamwise and spanwise scales are, on average, related.

Another conclusion of Naguib & Wark (1992), however, was that wall-layer eddies contribute more to the Reynolds stress near the wall than the large streamwise scales, based on uv estimates with filtered signals. Liu, Adrian & Hanratty (2001) also found the contribution of the large scales to decrease rapidly in the buffer layer. Above the buffer layer, however, large-scale motions *are* associated with Reynolds stress production. Proper orthogonal decomposition of a turbulent channel flow (Liu *et al.* 2001) showed that the set of large-scale modes that contributed significantly (50 %)

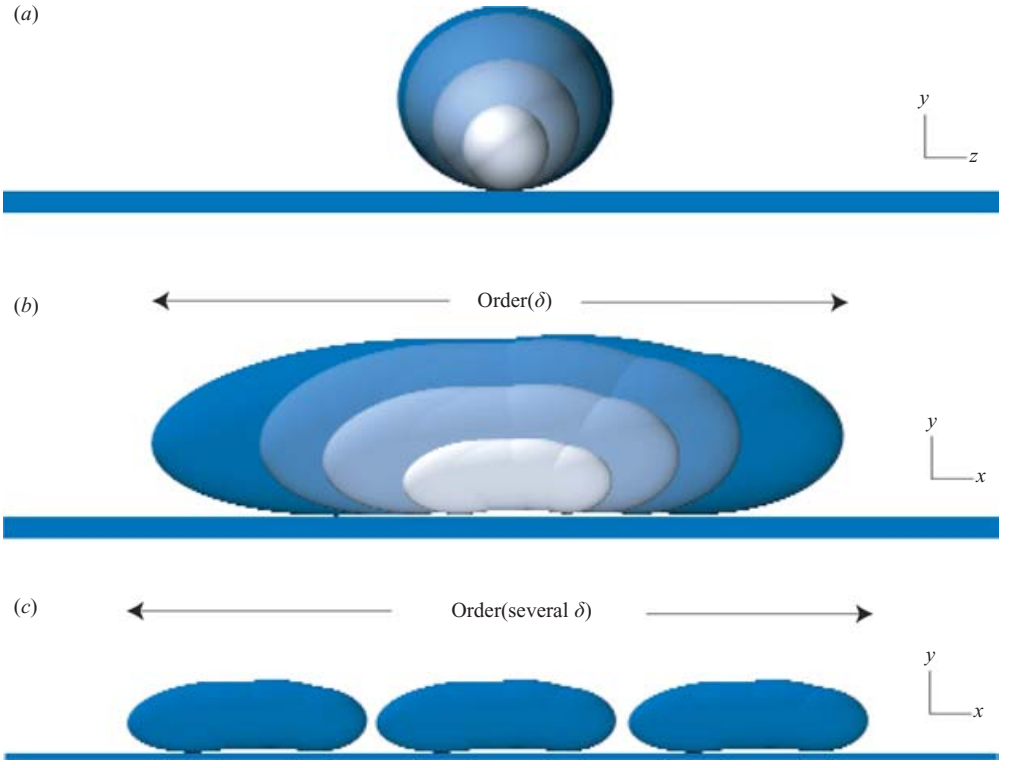

FIGURE 10. Highly idealized schematic depicting average growth of energetic motions in a boundary layer. (*a*) Idealized motions of multiple scales embedded within a δ-scale structure, viewed in the y–z-plane. Average growth in y and z is consistent with the attached-eddy hypothesis and continues until motions fill the layer spanwise. (*b*) Same set of idealized structures viewed in the x–y-plane. Motions grow self-similarly until spanwise growth saturates, after which streamwise growth continues. (*c*) Concatenation of multiple idealized δ-scale motions as a possible mechanism for formation of very-large-scale streamwise motions, viewed in the x–y-plane.

to the turbulent kinetic energy also contributed 75 % of the Reynolds shear stress above the buffer layer.

The vortex packet paradigm described in Adrian *et al.* (2000) again provides a framework for interpretation of these results. The coherent backwards induction created by the vortices in a packet forms a very long region of low u-momentum, which dominates the turbulent kinetic energy; it is considered 'large-scale'. This coherence is not present in the vertical component, however, leading to little contribution to uv from the lowest frequency motions. Close to the wall the Reynolds stress contribution occurs locally, on a scale associated with an individual wall-layer vortex, consistent with the results of Naguib & Wark (1992). At the same time, this vortex is one structure in a train of structures working cooperatively to create a larger-scale motion (again defined in terms of the streamwise component). Recent results by Ganapathisubramani, Longmire & Marusic (2003) support this concept. The authors apply a feature extraction algorithm to stereo PIV measurements in streamwise–spanwise planes of turbulent boundary layers. In the log region, the algorithm identifies regions as vortex packets and shows that the contribution of Reynolds stress per unit area in these regions is 5 to 7 times the average value. Thus, it appears

that the same set of structures that create the large-scale streamwise motions also contribute significantly to the Reynolds stress.

4. Conclusions

Large-scale motions leave strong imprints in two-dimensional power spectra of the streamwise component measured in x–z-planes throughout the logarithmic region of turbulent boundary layers. Low Reynolds number results ($Re_\theta = 1015$, $Re_\tau = 426$) reveal that peak spanwise energy resides in scales significantly larger than those associated with the established low-speed streak spacing, even near the wall: over 75 % of the energy is in scales larger than $\lambda_z^+ = 100$ at $y^+ \approx 21$. This result is consistent with the $Re_\tau = 400$ channel flow data of Liu *et al.* (1996). These complementary experiments measure different flows in separate facilities and are obtained with independent diagnostic systems, suggesting that these results are both reliable and universal. While the spanwise energy distribution of the smaller streamwise scales shows good agreement with visual streak spacing, it is shown that the large streamwise scales dominate the energy and are associated with larger spanwise scales; hence, the total spanwise energy peaks at larger scales ($\lambda_z^+ = 150$–300).

Large-scale outer-region structures with spacing $\lambda_z/\delta =$ 0.75–0.9 are shown to dominate the turbulent kinetic energy at the top of the logarithmic layer. The range of spanwise modes associated with these motions is found to be nearly constant over the Reynolds number range studied ($Re_\theta = 1015$ to 7705) when scaled with outer variables. One-dimensional spectra reveal that these motions remain highly energetic well into the logarithmic region at the high Re; for example, at $y^+ = 100$ ($y/\delta = 0.045$), over 50 % of the energy is in modes equal to or greater than ten times the distance from the wall ($\lambda_z^+ > 1000$). These large-scale structures are the streamwise-elongated low-momentum regions identified in Tomkins & Adrian (2003) and observed elsewhere (e.g. Wark & Nagib 1991), and are linked by Guezennec (1985) to Reynolds stress production.

The large-scale spanwise modes are associated with large-scale streamwise modes on average. The median spanwise energetic mode increases roughly linearly with increasing streamwise mode up to approximately $\lambda_{z,\mathrm{med}}/\delta = 0.8$, and then remains roughly constant for larger streamwise modes. The aspect ratio $\lambda_x/\lambda_{z,\mathrm{med}}$ decreases with increasing distance from the wall.

This research was supported by the Office of Naval Research under Grants N00014-99-1-188 and N00014-97-1-0109.

REFERENCES

Adrian, R. J. 1988 Statistical properties of particle image velocimetry measurements in turbulent flow. In *Laser Anemometry in Fluid Mechanics III* (ed. R. J. Adrian, T. Asauma, D. F. G. Durao, F. Durst & J. H. Whitelaw), pp. 115–129. Springer.

Adrian, R. J. 1991 Particle-imaging techniques for experimental fluid mechanics. *Annu. Rev. Fluid Mech.* **23**, 261–304.

Adrian, R. J. 1997 Dynamic ranges of velocity and spatial resolution of particle-image velocimetry. *Meas. Sci. Tech* **8**, 1393–1398.

Adrian, R. J., Meinhart, C. D. & Tomkins, C. D. 2000 Vortex organization in the outer region of the turbulent boundary layer. *J. Fluid Mech.* **422**, 1–54.

Del Alamo, J. C. & Jimenez, J. 2003 Spectra of the very large anisotropic scales in turbulent channels. *Phys. Fluids* **15**, L41–L44.

Del Alamo, J. C., Jimenez, J., Zandonade, P. & Moser, R. D. 2004 Scaling of the energy spectra of turbulent channels. *J. Fluid Mech.* **500**, 135–144.

Bendat, J. S. & Piersol, A. G. 1986 *Random Data: Analysis and Measurement Procedures*. John Wiley and Sons.

Christensen, K. T., Soloff, S. M. & Adrian, R. J. 2000 Piv sleuth: integrated particle image velocimetry (PIV) interrogation/validation software. *TAM Rep.* 943. Department of Theoretical and Applied Mechanics, University of Illinois at Urbana-Champaign.

Clauser, F. 1956 The turbulent boundary layer. *Adv. Appl. Mech.* **4**, 1–51.

Ganapathisubramani, B., Longmire, E. K. & Marusic, I. 2003 Characteristics of vortex packets in turbulent boundary layers. *J. Fluid Mech.* **478**, 35–46.

Guezennec, Y. G. 1985 Documentation of large coherent structures associated with wall-layer events in turbulent boundary layers. PhD thesis, Department of Mechanical Engineering, Illinois Institute of Technology, Chicago.

Head, M. R. & Bandyopadhyay, P. 1981 New aspects of turbulent boundary-layer structure. *J. Fluid Mech.* **107**, 297–338.

Kasagi, N. 1988 Structural study of near-wall turbulence and its heat transfer mechanism. In *Near-wall Turbulence* (ed. S. J. Kline & N. H. Afgan), pp. 596–619. Hemisphere.

Kim, K. C. & Adrian, R. J. 1999 Very large-scale motions in the outer layer. *Phys. Fluids* **11**, 417–422.

Kline, S. J., Reynolds, W. C., Schraub, F. A. & Runstadler, P. W. 1967 The structure of turbulent boundary layers. *J. Fluid Mech.* **30**, 741–773.

Kovasznay, L. S. G., Kibens, V. & Blackwelder, R. F. 1970 Large-scale motion in the intermittent region of a turbulent boundary layer. *J. Fluid Mech.* **41**, 283–325.

Krogstad, K. A. & Antonia, R. A. 1994 Structure of turbulent boundary layers on smooth and rough walls. *J. Fluid Mech.* **277**, 1–21.

Liu, Z.-C., Adrian, R. J. & Hanratty, T. J. 1996 A study of streaky structures in a turbulent channel flow with particle image velocimetry. In *Proc. 8th Intl Symp. on Appl. of Laser Tech. to Fluid Mech., Lisbon, Portugal* (ed. R. J. Adrian, D. F. G. Durao, F. Durst, M. V. Heitor, M. Maeda & J. H. Whitelaw). Springer

Liu, Z.-C., Adrian, R. J. & Hanratty, T. J. 2001 Large-scale modes of turbulent channel flow: transport and structure. *J. Fluid Mech.* **448**, 53–80.

McKeon, B. J., Li, J., Jiang, W. Morrison, J. F. & Smits, A. J. 2004 Further observations on the mean velocity distribution in fully developed pipe flow. *J. Fluid Mech.* **501**, 135–147.

McLean, I. R. 1990 The near wall eddy structure in an equilibrium turbulent boundary layer. PhD thesis, Department of Mechanical and Aerospace Engineering, University of Southern California, Los Angeles.

Meinhart, C. D. 1994 Investigation of turbulent boundary layer structure using particle-image velocimetry. PhD thesis, Department of Theoretical and Applied Mechanics, University of Illinois at Urbana-Champaign, Urbana.

Naguib, A. M. & Wark, C. E. 1992 An investigation of wall-layer dynamics using a combined temporal filtering and correlation technique. *J. Fluid Mech.* **243**, 541–560.

Nychas, S. G., Hershey, H. C. & Brodkey, R. S. 1973 A visual study of turbulent shear flow. *J. Fluid Mech.* **61**, 513–540.

Osterlund, J. M., Johansson, A. V., Nagib, H. M. & Hites, M. H. 2000 A note on the overlap region in turbulent boundary layers. *Phys. Fluids* **12**, 1–4.

Rajaee, M., Karlsson, S. & Sirovich, L. 1995 On the streak spacing and vortex roll size in a turbulent channel flow. *Phys. Fluids* **7**, 2439–2443.

Smith, C. R. 1984 A synthesized model of the near-wall behaviour in turbulent boundary layers. In *Proc. 8th Symposium of Turbulence* (ed. J. Zakin & G. Patterson), pp. 299–325. Univ. Missouri-Rolla, Rolla, Missouri.

Smith, C. R. & Metzler, S. P. 1983 The characteristics of low-speed streaks in the near-wall region of a turbulent boundary layer. *J. Fluid Mech.* **129**, 27–54.

Tomkins, C. D. & Adrian, R. J. 2003 Spanwise structure and scale growth in turbulent boundary layers. *J. Fluid Mech.* **490**, 37–74.

Townsend, A. A. 1976 *The Structure of Turbulent Shear Flow*, 2nd edn. Cambridge University Press.

Wark, C. E. & Nagib, H. M. 1991 Experimental investigation of coherent structures in turbulent boundary layers. *J. Fluid Mech.* **230**, 183–208.

Wark, C. E., Naguib, A. M. & Robinson, S. K. 1991 Scaling of spanwise length scales in a turbulent boundary layer. *AIAA Paper*. 91-0235.

Westerweel, J. 1997 Fundamentals of digital particle image velocimetry. *Meas. Sci. Tech.* **8**, 1379–1392.

Zagarola, M. V. & Smits, A. J. 1998 Mean-flow scaling of turbulent pipe flow. *J. Fluid Mech.* **379**, 33–79.